

# Non-Abelian chiral spin liquid on a simple non-Archimedean lattice

V. Peri,<sup>1</sup> S. Ok,<sup>2</sup> S. S. Tsirkin,<sup>2</sup> T. Neupert,<sup>2</sup> G. Baskaran,<sup>3,4</sup> M. Greiter,<sup>5</sup> R. Moessner,<sup>6</sup> and R. Thomale<sup>5,\*</sup>

<sup>1</sup>*Institute for Theoretical Physics, ETH Zurich, 8093 Zurich, Switzerland*

<sup>2</sup>*Department of Physics, University of Zurich, Winterthurerstrasse 190, 8057 Zurich, Switzerland*

<sup>3</sup>*Institute of Mathematical Sciences, Chennai 600 113, India*

<sup>4</sup>*Perimeter Institute for Theoretical Physics, Waterloo, Ontario N2L 2Y5, Canada*

<sup>5</sup>*Institute for Theoretical Physics and Astrophysics, University of Würzburg, Am Hubland, D-97074 Würzburg, Germany*

<sup>6</sup>*Max-Planck-Institut für Physik komplexer Systeme, Nöthnitzer Str. 38, 01187 Dresden, Germany*

(Dated: August 16, 2019)

We extend the scope of Kitaev spin liquids to non-Archimedean lattices. For the pentaheptite lattice, which results from the proliferation of Stone-Wales defects on the honeycomb lattice, we find an exactly solvable non-Abelian chiral spin liquid with spontaneous time reversal symmetry breaking due to lattice loops of odd length. Our findings call for potential extensions of exact results for Kitaev models which are based on reflection positivity, which is not fulfilled by the pentaheptite lattice. We further elaborate on potential realizations of our chiral spin liquid proposal in strained  $\alpha$ -RuCl<sub>3</sub>.

Since the first proposal<sup>1</sup>, quantum spin liquids have remained an as fascinating as elusive direction of contemporary condensed matter research on frustrated magnetism and topologically ordered many-body states. In theory, different approaches have been developed, many of which were inspired by cuprate superconductors<sup>2</sup> or the fractional quantum Hall effect (FQHE)<sup>3</sup>, but these were limited due to the relative paucity of exactly solvable models<sup>4,5</sup>. A fundamental breakthrough was reached by Kitaev in proposing a microscopic Hamiltonian for quantum spin liquids with an emergent massive Ising gauge theory<sup>6</sup>. Instead of just realizing a desired spin liquid ground state wave function as an exact eigenstate of a microscopic Hamiltonian, the powerful exact solution of the Kitaev spin liquid allows for the explicit analysis of anyonic excitations. Its solution is most elegantly accomplished by a Majorana representation, where the eigenspectrum simplifies to a free single-Majorana band structure.

The Kitaev models realize both Abelian and non-Abelian anyons<sup>6</sup>, spontaneous time reversal symmetry breaking chiral spin liquids<sup>7,8</sup>, a generalization to  $\mathbb{Z}_k$  gauge theory<sup>9</sup>, and an extension to three-dimensional spin liquids with anyon metallicity<sup>10–12</sup>. While the non-Abelian anyons in the Kitaev model are of Ising type, alternative microscopic approaches to non-Abelian spin liquids have found realizations of  $SU(2)_k$  anyons in chiral<sup>13–17</sup> and non-chiral<sup>18</sup> spin liquids. The concept of spinon Fermi surface has been previously developed in the context of Gutzwiller projections on fermionic mean field states<sup>19</sup>. The exact solvability of the Kitaev models, however, renders all these features accessible to an unprecedented degree, and as such promises a more concise connection to observable quantities<sup>20</sup> and candidate materials<sup>21–25</sup>.

In this Letter, we extend the Kitaev paradigm to non-Archimedean lattices. Lattices can be classified by the symmetry of sites and bonds. In Bravais lattices, all sites and bonds are equivalent. Archimedean lattices are formed by regular polygons where each lattice vertex is surrounded by the same sequence of polygons. This implies the equivalence of all sites, but not necessarily of all bonds. Conversely, for lattices of the type including the Lieb lattice<sup>26</sup>, the symmetry-equivalence of all bonds does not imply the equivalence of sites. In a non-Archimedean lattice, neither all sites nor all

bonds are equivalent. As a prototypical example to which we particularize in the following, pentaheptite (Fig. 1 (a)) exhibits irregular pentagons and heptagons as well as two types of vertices with  $(5^1, 7^2)$  and  $(5^2, 7^1)$  configuration, respectively. In this notation  $a^m$ , the lattice is characterized by a list of the number of edges  $a$  and the multiplicity  $m$  of polygons that surround each inequivalent vertex. Pentaheptite<sup>27,28</sup> can be thought of as originating from the honeycomb ( $6^3$ ) lattice by the proliferation of Stone-Wales defects. There, a pair of honeycomb bonded vertices change their connectivity as they rotate by 90 degrees with respect to the midpoint of their bond. The Stone-Wales defect proliferation transforms four contiguous hexagons into two heptagons and two pentagons. Pentaheptite has three-colorable bonds as the honeycomb lattice, and thus lends itself to an exact solution of the Kitaev model, albeit not being three-colorable by faces.

*Kitaev pentaheptite model* — We consider a spin-1/2 degree of freedom on each pentaheptite site. The unit cell shown in Fig. 1 (a) contains eight sites and is spanned by the vectors  $e_1 = (\sqrt{3}a, 3a)$  and  $e_2 = (\sqrt{3}a, -3a)$ . We set the nearest-neighbor distance  $a$  of the underlying honeycomb lattice to unity. The Kitaev Hamiltonian reads

$$H = -J_x \sum_{x\text{-type}} \sigma_j^x \sigma_k^x - J_y \sum_{y\text{-type}} \sigma_j^y \sigma_k^y - J_z \sum_{z\text{-type}} \sigma_j^z \sigma_k^z, \quad (1)$$

where  $\sigma_j^{x,y,z}$  denotes the Pauli matrices acting on site  $j$ , the sums run over distinct sets of bonds connecting nearest neighbor sites  $j$  and  $k$ , and  $J_{x,y,z} \in \mathbb{R}$ . Which bonds contribute to each sum is shown in Fig. 1 (a). Each heptagon and pentagon of the lattice is associated with a conserved quantity of (1) given by

$$\begin{aligned} W_{\text{pen}} &= K_{12}K_{23}K_{34}K_{45}K_{51}, \\ W_{\text{hep}} &= K_{12}K_{23}K_{34}K_{45}K_{56}K_{67}K_{71}, \end{aligned} \quad (2)$$

where  $K_{ij} = \sigma_i^\alpha \sigma_j^\alpha$  for sites  $i$  and  $j$  connected by a bond of type  $\alpha = x, y, z$ . The spin operators act on the sites around each pentagon and heptagon according to the site labels in Fig. 1 (b) and (c), respectively. The conserved quantities for the pentagons and heptagons that relate to those shown in

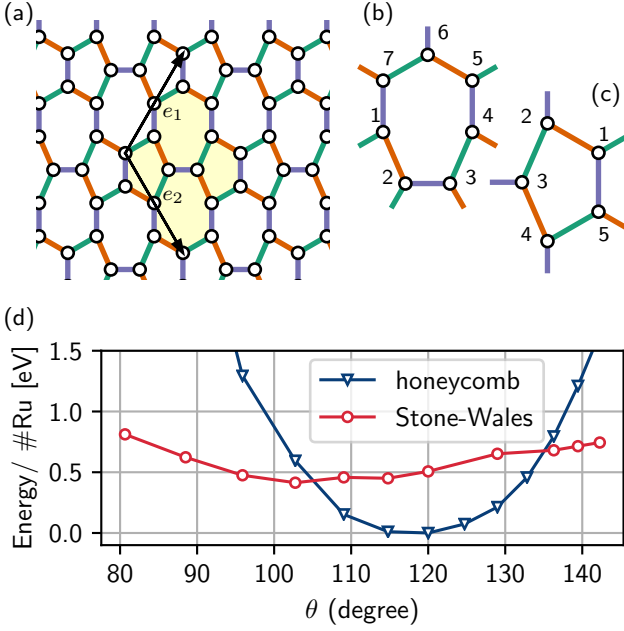


FIG. 1. (Color online) (a) pentaheptite lattice with a unit cell highlighted in light yellow and the lattice vectors  $e_1$  and  $e_2$ . The angle between the lattice vectors is  $\theta = 120^\circ$ . Bond colors highlight the type of spin-spin coupling across a bond  $\sigma_j^\alpha \sigma_k^\alpha$ ,  $\alpha = x, y, z$  (violet for  $z$ , orange for  $y$  and green for  $x$ ). (b),(c) site labels for the definition of plaquette operators in (2). (d) Energy per Ru atoms for  $\alpha$ -RuCl<sub>3</sub> under strain with respect to the energy of the honeycomb configuration at  $\theta = 120^\circ$ . In red for a honeycomb lattice, in blue for a Stone-Wales defect. The strain changes the angle  $\theta$  between the lattice vectors and the Stone-Wales structure is preferred at  $\theta < 105^\circ$  and  $\theta > 135^\circ$ .

Fig. 1 (b) and (c) via mirror reflection are defined analogously. All  $W_{\text{pen}}$  and  $W_{\text{hep}}$  commute with each other and the Hamiltonian (1), which can thus be diagonalized in each eigenspace of these operators (“flux sector”) separately.

Importantly, in contrast to the Kitaev honeycomb case, time-reversal  $T$  commutes with the plaquette operators  $W_l$  but flips their eigenvalues. Applying  $T$  to the equation  $W_l |\psi\rangle = w_l |\psi\rangle$ , one gets  $W_l T |\psi\rangle = w_l^* T |\psi\rangle$ . The reason is that the elementary loops in the pentaheptite lattice are of odd length and have imaginary eigenvalues  $\pm i$ . In particular, one needs to specify the direction followed around the plaquette and in definition (2) we choose a counterclockwise convention. A similar situation is found on the decorated honeycomb lattice (3, 12<sup>2</sup>) of the Kitaev-Yao-Kivelson (KYK) model<sup>7</sup>. This implies spontaneous time reversal symmetry breaking. In our case, however, *all* elementary loops are of odd length. The plaquette operators defined in (2) ensure that the composition law for fluxes holds<sup>29</sup>:  $W_{1+2} = W_1 W_2$ .

With the conserved plaquette quantities identified, one can map the system to noninteracting Majorana fermions in each flux sector by following Kitaev’s procedure<sup>6</sup>: we replace each spin (site  $j$ ) by four Majorana fermions  $c_j, b_j^\alpha$ ,  $\alpha = x, y, z$ , and restrict the Hilbert space to that of even fermion parity on

each site. The resulting Hamiltonian takes the form

$$H = \frac{i}{4} \sum_{\langle jk \rangle} A_{jk} c_j c_k, \quad (3)$$

where the sum runs over nearest-neighbor sites and  $A_{jk} = 2J_{\alpha_{jk}} u_{jk}$  if sites  $j$  and  $k$  are connected by an  $\alpha$  link,  $\alpha_{j,k} \in \{x, y, z\}$ . The Majorana bilinears  $u_{jk} = i b_j^{\alpha_{jk}} b_k^{\alpha_{jk}}$  commute with each other and the Hamiltonian. As Hermitian operators that square to 1, we can replace them by their eigenvalues  $\pm 1$ . Their eigenvalues are related to those of  $W_{\text{pen}}$  via

$$W_{\text{pen}} = (-i)^5 \prod_{\langle jk \rangle \in \text{pen}} u_{jk}, \quad (4)$$

where the product runs over all bonds that form a given pentagon. The analogous equation holds for  $W_{\text{hep}}$  with the prefactor  $(-i)^7$ . Thus, while the eigenvalue of  $u_{jk}$  on a given bond is gauge variant, the product of eigenvalues around a closed loop is a gauge invariant  $\mathbb{Z}_2$  flux. Note that the  $u_{jk}$  that share one index do not commute, and thus the order in the product of Eq. (4) matters<sup>30</sup>. According to our convention, the configuration with all the  $u_{ij}$  with positive eigenvalues corresponds to heptagonal (pentagonal) plaquettes with eigenvalue  $+i$  ( $-i$ ).

*Strain engineering of pentaheptite lattice in  $\alpha$ -RuCl<sub>3</sub>* — We perform first principle calculations of the candidate Kitaev honeycomb material  $\alpha$ -RuCl<sub>3</sub> under uniaxial strain (see Supplemental Material for more details). We find that under sufficiently strong tensile or compressive strain a configuration where the Ru atoms arrange themselves in a pentaheptite lattice becomes favorable (see Fig. 1 (d)). This result motivates our choice to extend the exactly solvable Kitaev model to non-Archimedean lattices.

*Identifying the ground state flux sector* — For each flux sector, the ground state energy of Eq. (3) can be determined. A powerful result by Lieb<sup>31</sup>, based on reflection positivity, assures that if a Kitaev-type spin model possesses reflection symmetry such that the plane of reflection does not contain any lattice site, a ground state is always in the flux free sector. The Kitaev model on the pentaheptite lattice is particular in that it does not have such a mirror symmetry.

From our flux sector analysis, we conjecture that even for Eq. (1), the ground state is in the flux free sector, i.e., the sector where all  $u_{ij}$  have positive eigenvalues according to the chosen convention. Numerical evidence along this line has been provided for other systems lacking reflection positivity, while a rigorous result is missing<sup>32</sup>. Fixing  $J_x = J_y = J_z = 1$  without loss of generality, we find the following: (i) For a cluster of  $2 \times 2$  unit cells, the energy computed for all vortex configurations<sup>30</sup> singles out the vortex-free sector with energy  $-3.1044$  per unit cell and an excitation gap of  $0.0026$ . The first excited sector is a cluster of  $\pi$  vortices in half of the plaquettes as displayed in Fig. 2 (b). (ii) Upon increasing system size, the energy of the vortex-free configuration extrapolates to  $-3.0971$  in the thermodynamic limit. (iii) The energy cost of nucleating a pair of vortices tends to a nonzero constant with increasing separation, indicating that it is not energetically favorable to nucleate isolated vortices [Fig. 2 (c)]. Based

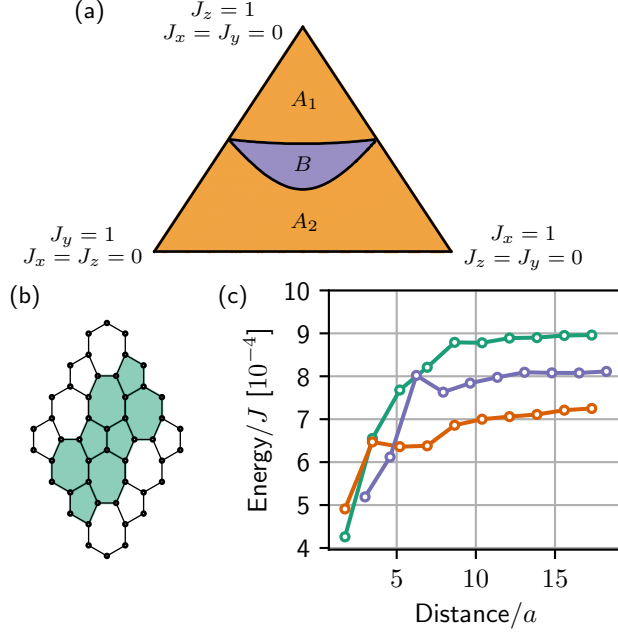


FIG. 2. (a) Phase diagram of the vortex-free sector of Hamiltonian (3). Phases  $A_1$  and  $A_2$  are topologically equivalent and realize the Abelian  $\mathbb{Z}_2$  topological order. Phase  $B$ , which includes the isotropic point, realizes the non-Abelian Ising topological order. (b) Flux configuration of lowest excited state for a system on the torus  $L_{e_1} \times L_{e_2}$  with  $L = 2$ . Colored plaquettes have flux  $\pi$ . (c) Energy cost per vortex for a pair of vortices as a function of their separation in a lattice on a torus with  $L = 10$  and  $J_x = J_y = J_z = J$ . For the green curve, vortices are in the pentagons. Vortices in heptagons are shown in orange. For the violet curve, one vortex is in a heptagon and the other in a pentagon.

on this numerical evidence, we consider the vortex-free sector for our subsequent analysis of the pentaheptite Kitaev spectrum.

**Phase diagram** — The state with all  $W_{\text{hep}} = +i$ ,  $W_{\text{pen}} = -i$  and that with  $W_{\text{hep}} = -i$ ,  $W_{\text{pen}} = +i$  are degenerate and related by time-reversal symmetry. Thus, in the vortex-free sector, the system spontaneously breaks time-reversal symmetry. Without loss of generality, we discuss the phases for  $J_{x,y,z} > 0$ , as the sign of the couplings is irrelevant: A change in the sign of  $J_x$  or  $J_y$  can be reabsorbed by changing the sign of an even number of  $u_{jk}$  per plaquette without adding vortices. At the same time,  $J_z < 0$  can be mapped to a configuration with  $J_z > 0$  and an odd number of  $u_{jk}$ 's per plaquette with flipped signs. This move adds a vortex in each plaquette, sending each configuration to its time reversed partner, and does not affect its energy<sup>30</sup>.

As shown in the ternary phase diagram Fig. 2 (a), we find three gapped phases, which are separated by phase boundaries given by

$$J_z^2 = J_x^2 \pm \sqrt{2}J_xJ_y + J_y^2. \quad (5)$$

Phases  $A_1$  and  $A_2$  are conveniently understood in a limit where one of the couplings  $J_x$ ,  $J_y$ , or  $J_z$  is much larger than the others. This is a good starting point for a perturbation

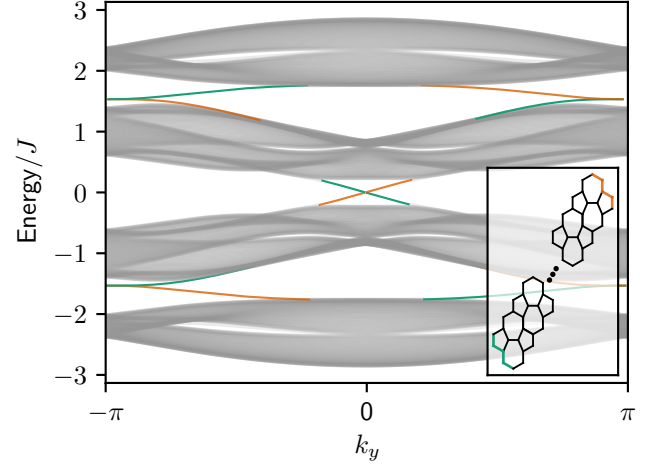


FIG. 3. Boundary spectrum of the flux free sector of model (1) for a ribbon with open boundary conditions along  $e_1$  and periodic along  $e_2$ , with  $J_x = J_y = J_z = J$ . The ribbon is composed of 50 unit cells along  $e_1$ . The Chern numbers of the three gaps are  $C = -1, +1, -1$  from bottom to top. Modes localized at one edge are plotted in green and those localized at the other edge in orange. The inset shows the edge terminations of the ribbon with respective colors.

theory in the Majorana fermion representation<sup>29</sup>. One finds<sup>30</sup> that only non-contractible loops give a flux-dependent correction to the energy. In particular, a loop with  $n$  weak bonds of strength  $J$  gives a correction of order  $J^n$ . Moreover, loops of odd length do not give any shift in energy as their contribution is cancelled by their time reversal partners. Assume  $J_z \gg J_x, J_y$  in  $A_1$ . The first non-trivial correction is given by the loops of length 10 involving adjacent pentagonal and heptagonal plaquettes. The Hamiltonian in sixth order perturbation theory reads

$$H_{\text{eff}}^{(6)} = \text{const.} - \frac{7}{128} \left( \frac{J_x^4 J_y^2}{|J_z|^5} + \frac{J_x^2 J_y^4}{|J_z|^5} \right) W_{\text{pen}} W_{\text{hep}}. \quad (6)$$

In  $A_2$ , assume  $J_y \gg J_x, J_z$  without loss of generality as the model is symmetric under  $J_x \leftrightarrow J_y$ . The first non trivial contribution arises in fourth order perturbation theory from the loops of length 8 involving two pentagons. This correction does not provide information on the energy cost of vortices in the heptagonal plaquettes. This enters in sixth order perturbation theory via the loops of length 10 enclosing a pentagon and a heptagon. The perturbative Hamiltonian up to sixth order for the phase  $A_2$  is:

$$H_{\text{eff}}^{(6)} = \text{const.} + \frac{5J_x^4}{16|J_y|^3} W_{\text{pen}} W_{\text{pen}'} - \frac{7J_x^2 J_z^4}{128|J_y|^5} W_{\text{pen}} W_{\text{hep}}. \quad (7)$$

From (6) and (7), we see that both in  $A_1$  and in  $A_2$  the vortex sector is gapped and the ground state is in the flux-free sector, i.e.,  $W_{\text{hep}} = +i$  and  $W_{\text{pen}} = -i$ . To study the vortex excitations, consider the phase  $A_1$  in the limit  $J_z \gg J_x, J_y$ . A

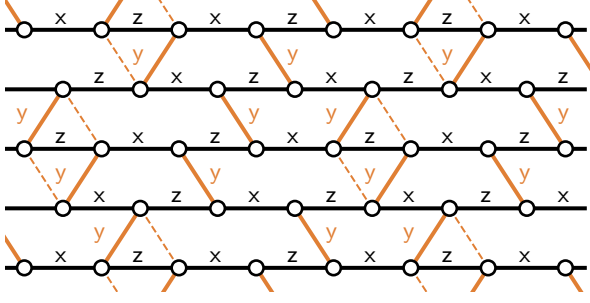


FIG. 4. Non-Abelian chiral spin liquid (phase  $B$ ) arising from weakly coupled spin chains. The Kitaev pentaheptite model can be deformed to an array of spin chains with alternating  $\sigma^x$ - $\sigma^x$  and  $\sigma^z$ - $\sigma^z$  coupling that are weakly coupled via  $\sigma^y$ - $\sigma^y$  interactions (orange lines). The dashed lines represent the  $\sigma^y$ - $\sigma^y$  interactions for the coupled wire construction of the honeycomb lattice.

pair of vortices can be created in two heptagonal plaquettes or in two pentagonal ones. The energy of these vortices shows little dependence on their separation. On the other hand, a single pair of vortices in a heptagon and a pentagon changes the fermionic parity and it is thus unphysical. These vortices do not carry unpaired Majorana modes. Similar results hold for the  $A_2$  phase. These observations, together with the four-fold ground state degeneracy, reproduce the fusion rules and the topological degeneracy of  $\mathbb{Z}_2$  topological order<sup>6</sup> and support the claim that these phases realize the same topological order as the same limit of Kitaev models on Archimedean lattices.

Phase  $B$ , which also contains the isotropic point  $J_x = J_y = J_z$ , is the chiral non-Abelian spin liquid. Our numerical studies suggest that both the vortex sector and the fermionic sector of this phase are gapped (see Supplemental Material and Fig. 2 (c)). Hence, vortices have well defined statistics. This can be entirely determined by the Chern number  $C$  associated to the Majorana spectrum according to the sixteen-fold way for Majorana fermions in a  $\mathbb{Z}_2$  background gauge field<sup>6</sup>. We find<sup>33</sup> that the spectral gap at half filling has  $|C| = 1$ . An odd Chern number is linked to non-Abelian statistics of the vortex excitation which carries an unpaired Majorana zero mode (MZM). In the presence of well isolated vortices, these MZMs can be resolved already via exact diagonalization. A pair of MZMs  $\{\gamma_i, \gamma_j\}$  can be used to construct a non-local fermionic degree of freedom  $a = 1/2(\gamma_i + i\gamma_j)$  with an associated two dimensional Fock space, such that a system of isolated  $2n$  vortices possess a topological degeneracy  $2^n$ . Taking into account the non-contractible loops on the torus and imposing fermionic parity conservation, the topological degeneracy for  $2n$  vortices in the  $B$  phase is  $2^{n+1}$ . The topological spin of the vortex excitation is  $\theta = \exp(\pm i\pi/8)$  and the associated quantum dimension  $d = \sqrt{2}$ . Therefore, the chiral non-Abelian spin liquid of the  $B$  phase is linked to Ising field theory. It is the same phase that can be induced by a magnetic field in Kitaev's model on the honeycomb lattice, albeit in this case at the cost of exact solvability<sup>6</sup>. Here, it is accompanied by a spontaneous breaking of time-reversal symmetry (by choosing all fluxes to be 0 or  $\pi$ ), as it is the

case in the KYK model on the  $(3, 12^2)$  Archimedean lattice in Ref. 7. Other possible realizations of this phase include the  $\nu = 5/2$  FQHE<sup>34</sup> and 2D topological superconductors<sup>35</sup>. The exact solubility of the model in the  $B$  phase offers the opportunity to study its chiral topological edge states for a geometry with open boundary conditions, as presented in Fig. 3. The boundary theory of the Ising topological order is a single chiral Majorana fermion mode, in accordance with  $|C| = 1$ .

*Coupled wire limit* — The limit  $J_z = J_x \gg J_y$  is particularly interesting to study the gapped non-Abelian chiral spin liquid phase. In this limit, (1) can be viewed as a collection of critical one-dimensional Ising chains with alternating  $x$ - and  $z$ -type terms (see Fig. 4) that are weakly coupled with  $y$ -type terms<sup>36,37</sup>. The same limit can be considered for the original Kitaev honeycomb model, which leads to a brick-wall lattice of weakly coupled chains. Thus, by merely changing the geometry of how the chains are connected, one can turn the gapless phase of the Kitaev honeycomb model into the gapped non-Abelian chiral spin liquid. The coupled wire picture highlights that with minimal changes to the hardware connectivity, one can go from the Abelian Kitaev honeycomb model to a non-Abelian Kitaev model. This represents one of the main advantages of the pentaheptite lattice over the KYK model. In fact, the latter cannot be obtained by a simple coupled wire construction, since in the non-Abelian limit  $J' \ll J$  (see Ref. 7), it consists of disconnected triangles. Recent ideas using Majorana-fermion based “topological hardware” offer a promising route toward realizing topologically ordered spin models (the “topological software”)<sup>38–40</sup>.

*Extensions to 3D* — Non-Archimedean lattices in three dimensions are abundant and go beyond the classification studied in Refs. 11 and 41. While we defer a detailed complete analysis to future work, it is interesting to notice how the pentaheptite lattice has a natural 3D extension in a three-coordinated lattice with elementary loops of odd length, e.g., the  $(9, 3)a$  lattice<sup>11</sup>. As such, it is amenable to an exact solution of the Kitaev model and spontaneously breaks time reversal symmetry, as the pentaheptite lattice in 2D. The Majorana spectrum of this model has Weyl points in the zero flux sector in the absence of external perturbations that explicitly break time reversal symmetry.

The  $(9, 3)a$  lattice has so far been understood mainly in terms of stacked honeycomb layers via mid-bond sites. It can, however, alternatively be obtained from the pentaheptite lattice by replacing the bonds shared by a pair of heptagons along  $e_1 - e_2$  with triangular spirals. The fact that the non-Archimedean 2D lattice studied here can originate from a simpler Archimedean 3D lattice may pave the way to candidate materials for this model which have not been considered previously, and stresses that non-Archimedean systems may generically arise from the dimensional reduction of an Archimedean parent lattice.

*Summary* — We have generalized the Kitaev spin liquid paradigm to non-Archimedean lattices, and find the Kitaev pentaheptite model to host an Ising-type non-Abelian chiral spin liquid. Towards a possible realization of this state of matter, we find that the Kitaev honeycomb material  $\alpha$ -RuCl<sub>3</sub> forms the pentaheptite lattice under uniaxial strain. A future

challenge will be to accomplish this experimentally, e.g., by substrate engineering; and, from a complementary theoretical point of view, to provide a microscopic derivation of the magnetic exchange interactions in the modified pentaheptite structure. More broadly, while there has been some systematic work on frustrated magnetism on Archimedean lattices<sup>42</sup>, a comparable effort on both Lieb-type and non-Archimedean lattices is still lacking, and we hope that our work will motivate such studies.

*Acknowledgments* — We thank Oleg Tchernyshyov for helpful comments and discussions. VP acknowledges support from the European Research Council under the Grant Agreement No. 771503 and NCCR MaNEP of the Swiss National Science Foundation. SO was supported by the Swiss National Science Foundation under grant 200021\_169061. TN and

SST acknowledge support from the European Unions Horizon 2020 research and innovation program (ERC-StG-Neupert-757867-PARATOP). GB acknowledges the support of the Wilhelm Wien institute as a distinguished Wilhelm Wien professor at the University of Würzburg, where this work was initiated, DST-SERB (India) for SERB Distinguished Fellowship and research at Perimeter Institute, as a DVRC, is supported by the Government of Canada through Industry Canada and by the Province of Ontario through the Ministry of Research and Innovation. The work in Würzburg and Dresden is funded by the Deutsche Forschungsgemeinschaft (DFG, German Research Foundation) through project-id 258499086 - SFB 1170, project-id 247310070 - SFB 1143, and through the Würzburg-Dresden Cluster of Excellence on Complexity and Topology in Quantum Matter – *ct.qmat* project-id 39085490 - EXC 2147.

- 
- \* rthomale@physik.uni-wuerzburg.de
- <sup>1</sup> P. Fazekas and P. W. Anderson, *The Philosophical Magazine: A Journal of Theoretical Experimental and Applied Physics* **30**, 423 (1974).
  - <sup>2</sup> P. W. Anderson, *Science* **235**, 1196 (1987).
  - <sup>3</sup> V. Kalmeyer and R. B. Laughlin, *Phys. Rev. Lett.* **59**, 2095 (1987).
  - <sup>4</sup> A. Kitaev, *Annals of Physics* **303**, 2 (2003).
  - <sup>5</sup> R. Moessner and S. L. Sondhi, *Phys. Rev. Lett.* **86**, 1881 (2001).
  - <sup>6</sup> A. Kitaev, *Annals of Physics* **321**, 2 (2006).
  - <sup>7</sup> H. Yao and S. A. Kivelson, *Phys. Rev. Lett.* **99**, 1 (2007).
  - <sup>8</sup> J. Fu, arXiv:1908.03123 (2019).
  - <sup>9</sup> M. Barkeshli, H.-C. Jiang, R. Thomale, and X.-L. Qi, *Phys. Rev. Lett.* **114**, 026401 (2015).
  - <sup>10</sup> M. Hermanns, K. O'Brien, and S. Trebst, *Phys. Rev. Lett.* **114**, 157202 (2015).
  - <sup>11</sup> K. O'Brien, M. Hermanns, and S. Trebst, *Phys. Rev. B* **93**, 1 (2016).
  - <sup>12</sup> J.-J. Miao, H.-K. Jin, F.-C. Zhang, and Y. Zhou, arXiv:1806.10960 (2018).
  - <sup>13</sup> M. Greiter and R. Thomale, *Phys. Rev. Lett.* **102**, 1 (2009).
  - <sup>14</sup> M. Greiter, D. F. Schroeter, and R. Thomale, *Phys. Rev. B* **89**, 1 (2014).
  - <sup>15</sup> T. Meng, T. Neupert, M. Greiter, and R. Thomale, *Phys. Rev. B* **91**, 1 (2015).
  - <sup>16</sup> P. Lecheminant and A. M. Tsvelik, *Phys. Rev. B* **95**, 140406 (2017).
  - <sup>17</sup> J.-Y. Chen, L. Vanderstraeten, S. Capponi, and D. Poilblanc, *Phys. Rev. B* **98**, 184409 (2018).
  - <sup>18</sup> B. Scharfenberger, R. Thomale, and M. Greiter, *Phys. Rev. B* **84**, 140404 (2011).
  - <sup>19</sup> O. I. Motrunich, *Phys. Rev. B* **72**, 045105 (2005).
  - <sup>20</sup> J. Knolle, D. L. Kovrizhin, J. T. Chalker, and R. Moessner, *Phys. Rev. Lett.* **112**, 207203 (2014).
  - <sup>21</sup> G. Jackeli and G. Khaliullin, *Phys. Rev. Lett.* **102**, 017205 (2009).
  - <sup>22</sup> Y. Singh *et al.*, *Phys. Rev. Lett.* **108**, 127203 (2012).
  - <sup>23</sup> K. W. Plumb *et al.*, *Phys. Rev. B* **90**, 041112 (2014).
  - <sup>24</sup> M. Hermanns, I. Kimchi, and J. Knolle, *Annu. Rev. Condens. Matter Phys.* **9**, 17 (2018).
  - <sup>25</sup> S. Trebst, arXiv:1701.07056 (2017).
  - <sup>26</sup> E. H. Lieb, *Phys. Rev. Lett.* **62**, 1201 (1989).
  - <sup>27</sup> V. H. Crespi, L. X. Benedict, M. L. Cohen, and S. G. Louie, *Phys. Rev. B* **53**, R13303 (1996).
  - <sup>28</sup> M. Deza, P. W. Fowler, M. Shtogrin, and K. Vietze, *Journal of Chemical Information and Computer Sciences* **40**, 1325 (2000).
  - <sup>29</sup> O. Petrova, P. Mellado, and O. Tchernyshyov, *Phys. Rev. B* **90**, 134404 (2014).
  - <sup>30</sup> see Supplemental Material at. (unpublished).
  - <sup>31</sup> E. H. Lieb, *Phys. Rev. Lett.* **73**, 2158 (1994).
  - <sup>32</sup> S. Chesi, A. Jaffe, D. Loss, and F. L. Pedrocchi, *J. Math. Phys.* **54**, (2013).
  - <sup>33</sup> T. Fukui, Y. Hatsugai, and H. Suzuki, *J. Phys. Soc. Jpn.* **74**, 1674 (2005).
  - <sup>34</sup> G. Moore and N. Read, *Nucl. Phys. B* **360**, 362 (1991).
  - <sup>35</sup> D. A. Ivanov, *Phys. Rev. Lett.* **86**, 268 (2001).
  - <sup>36</sup> P.-H. Huang *et al.*, *Phys. Rev. B* **93**, 205123 (2016).
  - <sup>37</sup> P.-H. Huang *et al.*, *Phys. Rev. B* **95**, 144413 (2017).
  - <sup>38</sup> E. Sagi *et al.*, *Phys. Rev. B* **99**, 075107 (2019).
  - <sup>39</sup> L. A. Landau *et al.*, *Phys. Rev. Lett.* **116**, 050501 (2016).
  - <sup>40</sup> S. Plugge *et al.*, *Phys. Rev. B* **94**, 1 (2016).
  - <sup>41</sup> A. Wells, *Three dimensional nets and polyhedra*, *Wiley monographs in crystallography* (Wiley, 9780471021513, 1977).
  - <sup>42</sup> D. J. J. Farnell *et al.*, *Phys. Rev. B* **89**, 184407 (2014).
  - <sup>43</sup> F. L. Pedrocchi, S. Chesi, and D. Loss, *Phys. Rev. B* **84**, 1 (2011).
  - <sup>44</sup> G. Kresse and J. Hafner, *Phys. Rev. B* **48**, 13115 (1993).
  - <sup>45</sup> G. Kresse and J. Furthmüller, *Computational Materials Science* **6**, 15 (1996).
  - <sup>46</sup> P. E. Blöchl, *Phys. Rev. B* **50**, 17953 (1994).
  - <sup>47</sup> G. Kresse and D. Joubert, *Phys. Rev. B* **59**, 1758 (1999).
  - <sup>48</sup> J. P. Perdew, K. Burke, and M. Ernzerhof, *Phys. Rev. Lett.* **77**, 3865 (1996).

# Non-Abelian chiral spin liquid on a simple non-Archimedean lattice

## Supplemental Material

V. Peri,<sup>1</sup> S. Ok,<sup>2</sup> S. S. Tsirkin,<sup>2</sup> T. Neupert,<sup>2</sup> G. Baskaran,<sup>3,4</sup> M. Greiter,<sup>5</sup> R. Moessner,<sup>6</sup> and R. Thomale<sup>5</sup>

<sup>1</sup>*Institute for Theoretical Physics, ETH Zurich, 8093 Zurich, Switzerland*

<sup>2</sup>*Department of Physics, University of Zurich, Winterthurerstrasse 190, 8057 Zurich, Switzerland*

<sup>3</sup>*Institute of Mathematical Sciences, Chennai 600 113, India*

<sup>4</sup>*Perimeter Institute for Theoretical Physics, Waterloo, Ontario N2L 2Y5, Canada*

<sup>5</sup>*Institute for Theoretical Physics and Astrophysics, University of Würzburg, Am Hubland, D-97074 Würzburg, Germany*

<sup>6</sup>*Max-Planck-Institut für Physik komplexer Systeme, Nöthnitzer Str. 38, 01187 Dresden, Germany*

(Dated: August 16, 2019)

### Physical subspace projection

The states obtained in the Majorana representation are projected to the physical subspace formed by  $|\psi\rangle$ s that satisfy  $D_i |\psi\rangle = |\psi\rangle$  for each site index  $i$ , where  $D_i = b_i^x b_i^y b_i^z c_i$ . The projector on the physical subspace can be written as:

$$\mathcal{P} = \prod_{i=1}^{8N} \left( \frac{1 + D_i}{2} \right), \quad (1)$$

where  $N$  is the number of unit cells in the system. As highlighted in Ref. 43, unphysical states can likewise be characterized by the positive eigenvalue of the operator  $\prod_{i=1}^{8N} D_i$ , which is more convenient to compute. Restricting our attention to physical states, each configuration of the system with periodic boundary conditions is entirely characterized by the eigenvalues of the elementary plaquette operators and two additional numbers  $(\phi_x, \phi_y)$ . These are two global  $\mathbb{Z}_2$  fluxes computed along a contour that crosses the whole sample along  $x$  and  $y$ , respectively.

### DFT calculations of $\alpha$ -RuCl<sub>3</sub>

The structural relaxation and total-energy calculations of  $\alpha$ -RuCl<sub>3</sub> under uniaxial strain was performed within the framework of density functional theory (DFT) with the scalar-relativistic approximation. The calculation is done using the VASP code<sup>44,45</sup> employing the projector-augmented wave method (PAW)<sup>46,47</sup> and the Perdew, Burke, and Ernzerhof generalized-gradient approximation (GGA-PBE)<sup>48</sup> for the exchange-correlation functional. We start from the honeycomb lattice of  $\alpha$ -RuCl<sub>3</sub> monolayer with equilibrium lattice parameter, and then change the angle  $\theta$  between the unit cell vectors, simultaneously adjusting the lattice parameter to keep the surface of the 2D unit cell fixed. For each value of  $\theta$ , all atoms are relaxed to their equilibrium positions inside the unit cell, yielding the minimal total energy. Further, we take a  $2 \times 2$  supercell to introduce one Stone-Wales (SW) defect and relax the structure for different values of the stretching angles  $\theta$ , in the same way as for the honeycomb lattice.

The resulting total energies are shown in Fig. 1 (a) of the Main Text. One can see that at  $\theta = 120^\circ$  the honeycomb lattice is energetically preferred over the Stone-Wales structure. We take the minimum energy of the honeycomb structure as a reference point for Fig. 1 (a) of the Main Text. As we change the angle  $\theta$  from  $120^\circ$ , the energy sharply increases. On the other hand, the energy of the SW structure has a weaker dependence on the angle, and thus becomes energetically preferred at  $\theta < 105^\circ$  and  $\theta > 135^\circ$ . Moreover, the equilibrium angle for this structure is around  $102^\circ$ , which gives a hope for an experimental realization. The atomic structures for  $\theta = 136^\circ$  and  $\theta = 96^\circ$  are shown in Fig. 1 (a) and (b), respectively.

Under sufficient strain, the pentaheptite lattice studied in this work is favorable. Although the DFT calculations have been performed on the candidate Kitaev material  $\alpha$ -RuCl<sub>3</sub>, it is not obvious whether Kitaev-like exchanges continue to be relevant. The number of Ru atoms and octahedral Cl cages surrounding them is preserved during the distortion. The odd loops, however, introduce frustration in the structure and the octahedral cages cannot always share one edge. This can be appreciated in Fig. 1 (b), where the two octahedral cages in the distorted bond get separated. The determination of the extent to which this frustration is detrimental to the directional Kitaev exchange goes beyond the scope of this work.

### Convention for bond orientation

Majorana operators satisfy the anticommutation relations  $\{b_i^\alpha, b_j^\alpha\} = 0$  for  $i \neq j$ . Thus, the Majorana bilinears  $u_{jk} = ib_j^{\alpha_{jk}} b_k^{\alpha_{jk}}$  are odd under index permutation:  $u_{jk} = -u_{kj}$ . Note that  $u_{jk}$ s that share one index do not commute, and the order in the product of Eq.(4) of Main Text matters. This forces us to choose an arbitrary convention for the orientation of the bonds. The convention adopted throughout this work is presented in Fig. 2, where the  $u_{jk}$  are taken positive in the arrow's direction. Note how, in accordance with Eq.(2) of Main Text, each loop contains an even number of bonds directed clockwise.



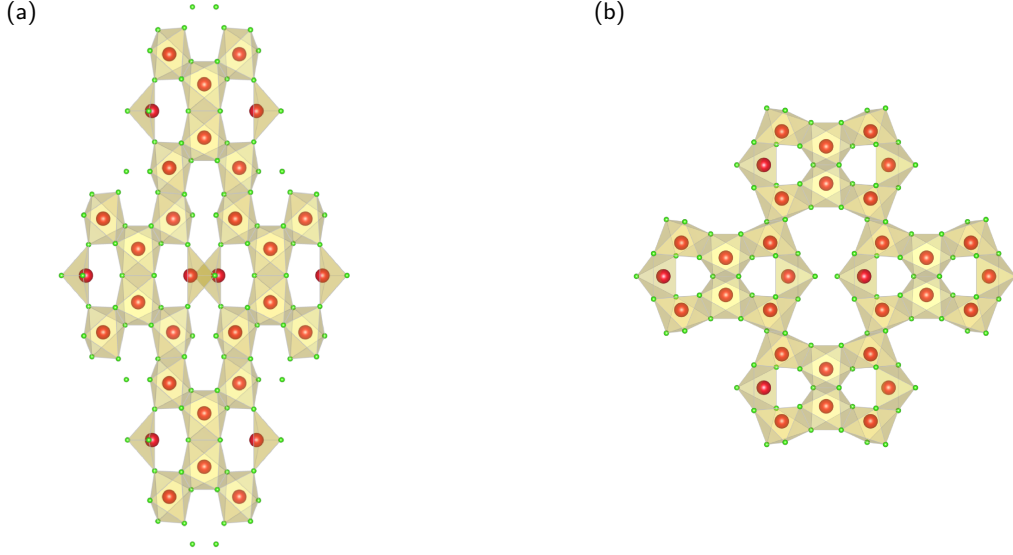


FIG. 1. Crystal structure of the Kitaev material  $\alpha$ -RuCl<sub>3</sub> under strain. (a) Angle between lattice vectors  $\theta = 136^\circ$ . (b) Angle between lattice vectors  $\theta = 96^\circ$ .

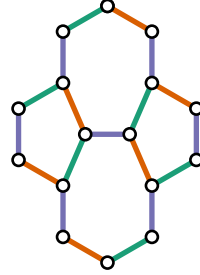


FIG. 2. Unit cell with arrows indicating the positive orientation of the bilinears  $u_{jk}$ . Bond colors highlight the type of spin-spin coupling across a bond  $\sigma_j^\alpha \sigma_k^\alpha$ ,  $\alpha = x, y, z$  (violet for  $z$ , orange for  $y$  and green for  $x$ ).

### Effects of the couplings sign

As argued in the Main Text, the sign of the couplings has no effects on the energy of the system. A change in the sign of  $J_x$  or  $J_y$  can be reabsorbed changing the sign of an even number of  $u_{jk}$ , leaving the eigenvalues of  $W_p$  unchanged and without exiting the flux sector. At the same time, the model with a negative  $J_z$  can be mapped to a configuration with a positive coupling and an odd number of  $u_{jk}$ s with flipped signs per plaquette. This maps each flux sector to its time reversal partner and does not change the energy.

A change of sign can however affect other quantities. For example, changing the sign of  $J_z$  changes the sign of the Chern number in each gap of the spectrum. In fact, the time reversal operation that absorbs the change  $J_z \rightarrow -J_z$  flips the sign of the Chern number. In Fig. 3, we show how the same system with different signs of  $J_z$  has edge modes propagating in opposite directions.

### Majorana Fermi surface

The free-fermions tight-binding model on a pentaheptite lattice has a metallic character. The Fermi surface at half filling is shown in Fig. 4 (a). On the other hand, in the zero flux sector of the Kitaev model, the single particle Majorana spectrum is gapped. One may wonder whether there are simple flux configurations that close the gap and induce a Majorana Fermi surface. We answer such question in the affirmative. In particular, the flux configuration that breaks  $C_2$  symmetry and preserves the full

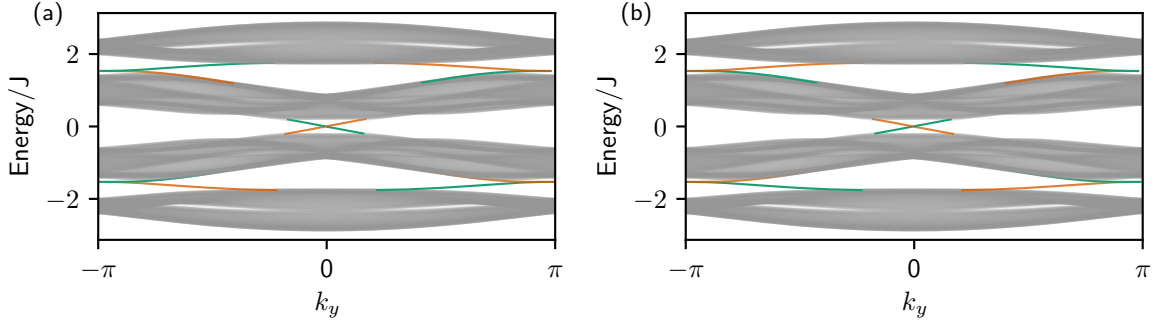


FIG. 3. Boundary spectrum of the flux free sector for a ribbon with open boundary conditions along  $e_1$  and periodic along  $e_2$ , with  $J_x = J_y = |J_z| = J$ . The ribbon is composed of 50 unit cells along  $e_1$ . In orange the modes located on the edge with normal  $+e_1$  and in green edge modes located on the opposite edge. (a)  $J_z > 0$  (as in the Main Text), the Chern numbers of the three gaps are  $C = -1, +1, -1$  from bottom to top. (b)  $J_z < 0$ , the Chern numbers of the three gaps are  $C = +1, -1, +1$  from bottom to top. In the two cases, edge modes on the same surface propagate in opposite directions.

lattice translation symmetry, without enlarging the unit cell, achieves this goal. With a  $\pi$  flux in a heptagon and a pentagon of the unit cell, the spectrum develops a Majorana Fermi surface, as shown in Fig. 4 (b).

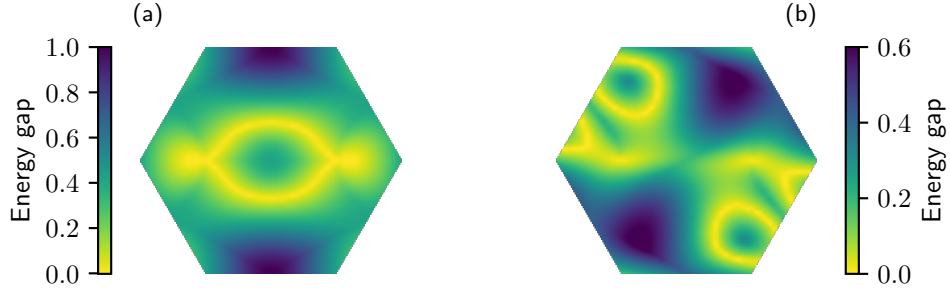


FIG. 4. Fermi surface in the first Brillouin zone. The plot shows the minimum of the absolute value of the eigenvalues in the first Brillouin zone of the pentaheptite lattice and the line of zero energy defines the Fermi surface. (a) Free-Fermions. (b) Free-Majoranas in the presence of  $\pi$  flux in a pentagon and a heptagon of the unit cell. In both cases  $J_x = J_y = J_z = J$ .

#### Perturbation theory in the $A_1$ and $A_2$ phases

Phases  $A_1$  and  $A_2$  are conveniently understood in a limit where one of the couplings  $J_x$ ,  $J_y$ , or  $J_z$  is much larger than the others. This is a good starting point for a perturbation theory in the Majorana fermion representation. Compared to the Rayleigh-Schrödinger perturbation theory for spins, the same analysis in the fermionic representation can be formulated in the Feynman diagrams language<sup>29</sup>. This results in few simple diagrammatic rules. For sake of concreteness, we consider the case  $J_z \gg J_x = J_y$  and present the rules in this limit. (i) Construct all possible closed paths involving weak and strong bonds. (ii) Compute the amplitude of the path. Each weak bond  $ij$  contributes a factor  $2J_x u_{ij}$ . Each strong bond contributes a factor  $2J_z u_{ij} / (\omega^2 + (2J_z)^2)$ . Each strong bond attached to the path with only one site gives a factor  $\omega / (\omega^2 + (2J_z)^2)$ . Give an extra factor  $1/2$  and integrate over the whole frequency range  $-\infty \leq \omega \leq +\infty$ . (iii) Sum over all possible paths considering the reverse of a non-contractible path as a different one.

Few observations can be readily drawn from these rules. Self-retracting paths gives energy contributions that are flux independent. In fact, each bond  $ij$  appears twice giving a constant contribution:  $u_{ij}u_{ji} = -1$ . Non-trivial contributions are given by non-contractible loops. Among those, only the even length ones contribute. In fact, since  $u_{ij} = -u_{ji}$ , loops of odd length followed in opposite directions result in opposite sign contributions that cancel each other. A closed loop with  $n$  weak bonds will give a contribution of order  $J_x^n$ . The amplitude of a path of length  $\ell$  is a positive number times  $(+i)^\ell W_\ell$ . We now focus our attention on non-self-retracting loops that give the first non-trivial corrections in the perturbative Hamiltonians for the  $A_1$  and  $A_2$  phases of the Kitaev model on the pentaheptite lattice.

For the  $A_1$  phase, we consider the limit  $J_z \gg J_x, J_y$  and all positive couplings. The lowest order flux-dependent contribution is given by the loops of length 10 enclosing a pentagon and a heptagon. There are two inequivalent loops of this type per unit



cell, each with double multiplicity (see Fig. 5). The contribution from the loop of Fig. 5 (a) is:

$$-2 \times 2 \int_{-\infty}^{\infty} \frac{d\omega}{2\pi} \frac{1}{2} (2J_x)^4 (2J_y)^2 \frac{\omega}{\omega^2 + (2J_z)^2} \frac{\omega}{\omega^2 + (2J_z)^2} \frac{(2J_z)^4}{(\omega^2 + (2J_z)^2)^4} W_5 W_7 = -\frac{7J_x^4 J_y^2}{128J_z^5} W_5 W_7, \quad (2)$$

where a factor 2 comes from the same loop traversed in opposite direction and another factor 2 from the presence of two different loops of this type per unit cell. Here we use  $W_{10} = W_5 W_7$ , according to our definition of the plaquette operators (see Main Text). The contribution from the similar loop of Fig. 5 (b) reads:

$$-2 \times 2 \int_{-\infty}^{\infty} \frac{d\omega}{2\pi} \frac{1}{2} (2J_x)^2 (2J_y)^4 \frac{\omega}{\omega^2 + (2J_z)^2} \frac{\omega}{\omega^2 + (2J_z)^2} \frac{(2J_z)^4}{(\omega^2 + (2J_z)^2)^4} W_5 W_7 = -\frac{7J_x^2 J_y^4}{128J_z^5} W_5 W_7. \quad (3)$$

Summing all these terms with the correct multiplicity, we get the sixth order effective Hamiltonian for the  $A_1$  phase:

$$H_{\text{eff}}^{(6)} = \text{const.} - \frac{7}{128} \left( \frac{J_x^4 J_y^2}{J_z^5} + \frac{J_x^2 J_y^4}{J_z^5} \right) W_5 W_7. \quad (4)$$

A similar analysis can be performed for the phase  $A_2$  in the limit  $J_y \gg J_x, J_z$ . The lowest order non-contractible loop is of length 8 and encloses two pentagons, Fig. 5 (d). It gives a fourth order contribution:

$$2 \int_{-\infty}^{\infty} \frac{d\omega}{2\pi} \frac{1}{2} (2J_x)^4 \frac{(2J_y)^4}{(\omega^2 + (2J_y)^2)^4} W_5 W_{5'} = \frac{5J_x^4}{16J_y^3} W_5 W_{5'}, \quad (5)$$

where the factor 2 comes from the two orientations of the loop and we used  $W_8 = W_5 W_{5'}$ . Eq. (5) gives the dominant energy cost for an isolated vortex in a pentagonal plaquette. It does not, however, determine the energy cost of a vortex in a heptagonal plaquette. Hence, we need to consider sixth order contributions given by loops of length 10 enclosing a pentagon and a heptagon (see Fig. 5 (c)). The contribution of such loops is given by:

$$-2 \times 2 \int_{-\infty}^{\infty} \frac{d\omega}{2\pi} \frac{1}{2} (2J_x)^2 (2J_z)^4 \frac{\omega}{\omega^2 + (2J_y)^2} \frac{\omega}{\omega^2 + (2J_y)^2} \frac{(2J_y)^4}{(\omega^2 + (2J_y)^2)^4} W_5 W_7 = -\frac{7J_x^2 J_y^4}{128J_z^5} W_5 W_7, \quad (6)$$

similarly to Eq. (2). Summing all contributions gives the sixth order perturbative Hamiltonian for the  $A_2$  phase:

$$H_{\text{eff}}^{(6)} = \text{const.} + \frac{5J_x^4}{16J_y^3} W_5 W_{5'} - \frac{7J_x^2 J_z^4}{128J_y^5} W_5 W_7. \quad (7)$$

Note that in the vortex-free sector all heptagonal plaquettes have eigenvalue  $+i$  and the pentagonal ones  $-i$ . Hence, in sixth order perturbation theory, isolated vortices have a finite energy cost over the ground state energy in phase  $A_1$  and  $A_2$ .

### Topological phases degeneracy

We checked the degeneracies of the different topological phases in the vortex-free sector. Only physical state with fixed fermionic parity have been considered. In the  $A_1$  and  $A_2$  phases, we find a four-fold degeneracy of the ground state on a torus. This is consistent with the Abelian topological phase of  $\mathbb{Z}_2$  topological order. The four different ground states (GS) are fully characterized by the  $\mathbb{Z}_2$  global fluxes  $(\phi_x, \phi_y)$  around the handles of the torus. In the non-Abelian phase  $B$ , the GS degeneracy is threefold, compatible with an Ising topological field theory. One of the flux-free sectors of the non-Abelian phase does not belong to the physical subspace (with our convention, the state  $(0, 0)$  does not belong to the physical subspace).

It is important to stress how the exact GS degeneracy is present only in the thermodynamic limit. For example, on the torus  $L_{e_1} \times L_{e_2}$  the three GS of the non-Abelian phase have considerably different energies for  $L = 2$ . For  $J_x = J_y = J_z = J$ , the energy per unit cell in units of  $J$  is:

- (1,0): -3.1044
- (0,1): -3.1044
- (1,1): -3.0892

The first excited state has lower energy than the vortex-free configuration (1, 1). However, for  $L = 10$  the system is already large enough to show a convergence of the energies of the vortex-free states:

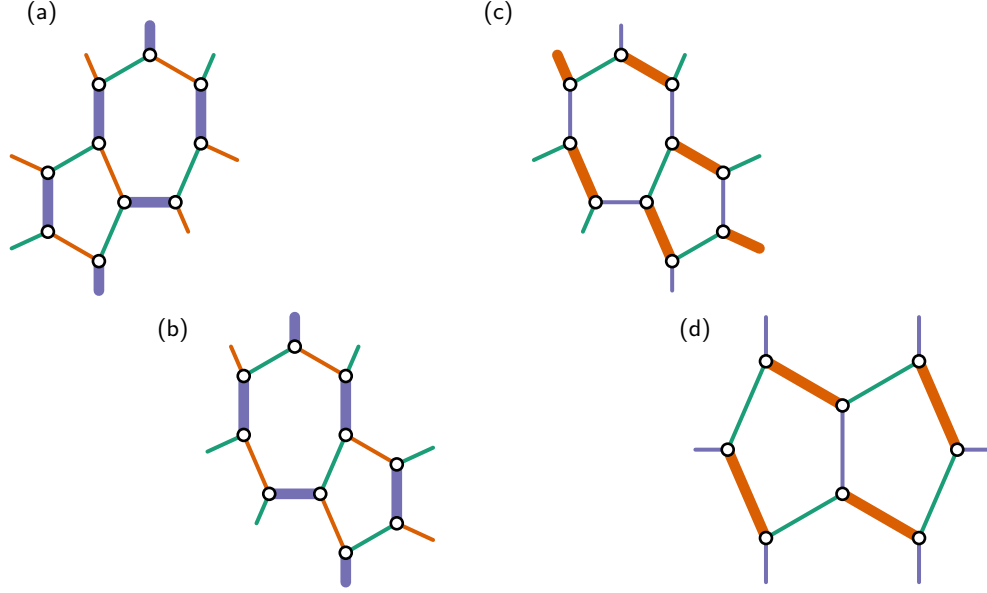


FIG. 5. Non-self-retracting paths on the pentaheptite lattice. The thickness of the bond is proportional to the coupling strength. Bond colors highlight the type of spin-spin coupling across a bond  $\sigma_j^\alpha \sigma_k^\alpha$ ,  $\alpha = x, y, z$  (violet for  $z$ , orange for  $y$  and green for  $x$ ). (a)–(b) Inequivalent loops of length 10 that give the sixth order perturbation Hamiltonian for the  $A_1$  phase. (c) Loop of length 10 that gives the sixth order contribution to the perturbative Hamiltonian in the phase  $A_2$ . (d) Loop of length 8 that gives the flux-dependent fourth order contribution.

- (1,0): -3.097073
- (0,1): -3.097073
- (1,1): -3.097072

### Vortex energies

We studied in further details the vortex sector in the  $B$  phase. The nucleation of a well isolated vortex costs a non-zero amount of energy. However, a pair of vortices close to each others has little energy cost and it suggests the existence of an attractive force between vortices that could favor the formation of clusters. We study the energy cost of clusters on a torus  $Le_1 \times Le_2$  with  $L = 10$  and  $J_x = J_y = J_z = J$ . In Fig. 6 (b) we see how the energy cost per vortex decreases while the cluster size increases. This seems to point to the existence of a GS different from the vortex-free one. However, Fig. 6 (a) shows the finite energy gap between the vortex-free sector and the configuration with a vortex cluster. The decrease in energy cost per single vortex is not enough to compensate the increasing number of vortices in the cluster. Therefore, the formation of large clusters is not favored. As a last evidence, in Fig. 6 (c), we calculate the cost per unit length of the domain wall between the cluster and the rest of the system. This quantity fluctuates around a constant non-zero value and suggests the existence of a finite energy cost to create a domain wall. All these results seem to validate the assumption of the vortex-free flux sector as ground state. These findings call for potential extensions of exact results for Kitaev models which are based on reflection positivity, which is not fulfilled by the pentaheptite lattice.

### Edge modes

In Fig. 7 (a) we show the spectrum of a ribbon for the Abelian phase  $A_2$ . There are no chiral Majorana modes crossing the band gap around zero energy.

The non-Abelian phase  $B$  is characterized by  $|C| = 1$  and a chiral Majorana edge mode crosses the zero energy gap, as shown in Fig. 3. In Fig. 7 (b), we show the localization of these modes at the boundary of the ribbon.

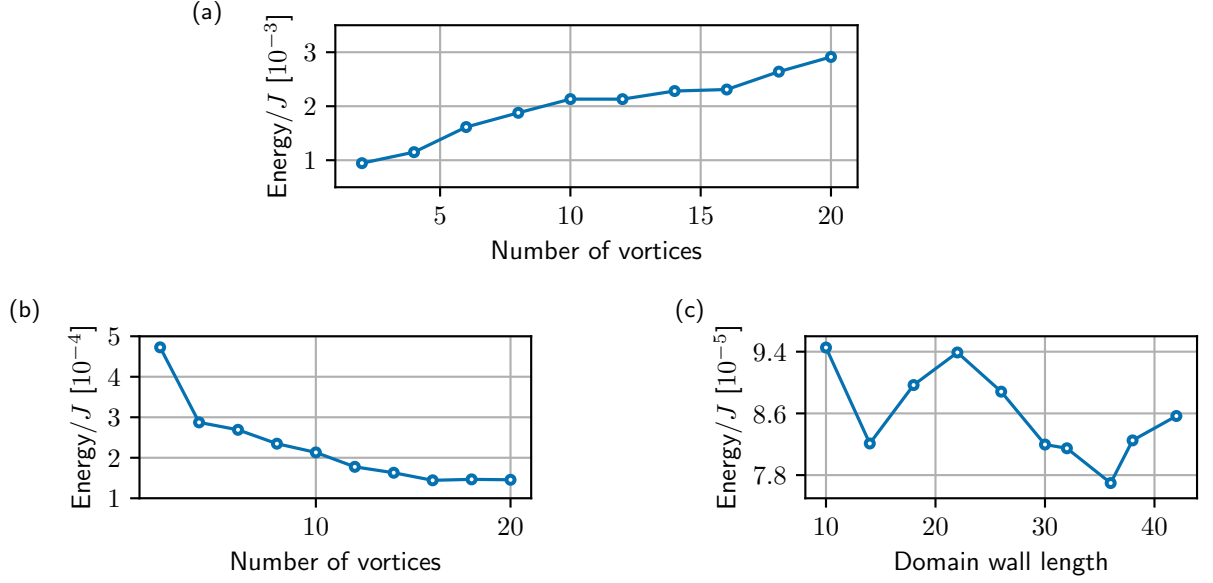


FIG. 6. Energy cost for vortex clusters of different sizes. (a) Global energy cost over the vortex-free flux sector as a function of the number of vortices in the cluster. (b) Energy cost per single vortex as a function of the number of vortices in the cluster. (c) Energy cost for unit length of cluster's domain wall.

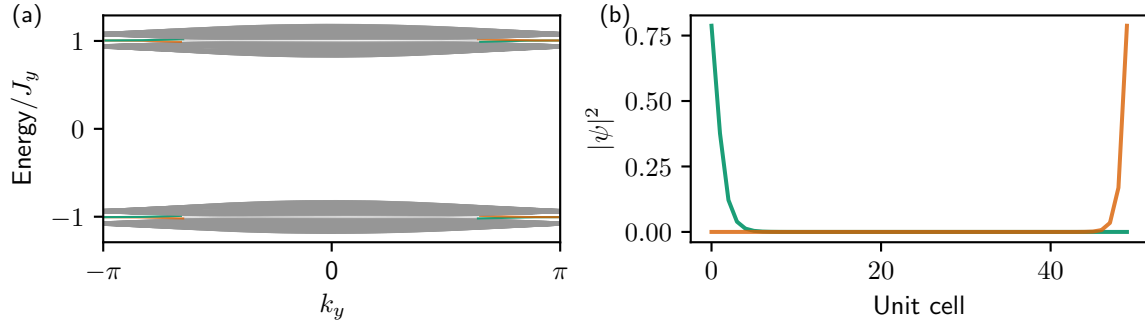


FIG. 7. (a) Boundary spectrum of the vortex-free sector in the Abelian phase  $A_2$  for a ribbon with open boundary conditions along  $e_1$  and periodic along  $e_2$ , with  $J_y = 1$ ,  $J_z = J_x = 0.1$ . The ribbon is composed of 50 unit cells along  $e_1$ . There are no edge modes crossing the zero energy single-particle gap. (b) Square modulus of the wavefunctions for the edge modes in Fig. 3 of Main Text. The green state is strongly localized on the edge with normal  $-e_1$ , while the orange mode is localized on the opposite edge.